**Supplementary Materials**

# Self-limited atomic-layer tin-sulfides with high-electron-intensity interface induced ultrathin SEI for fast-charging sodium-ion batteries

**Jingjing Gai[1,8,#], Keming Song[1,8,#], Rui Pang[2,8,#], Lingmei Liu[3,8,#], Hongliu Dai[4], Haiying Du[1], Tingting Yang[5], Shunfang Li[2], Shuhui Sun[4], Qi Liu[5], Yuliang Cao[6], Yu Han[3], Weihua Chen[1,7,*]**

[1]College of Chemistry, Zhengzhou University, Zhengzhou 450001, Henan, China.
[2]School of Physics and Engineering, Zhengzhou University, Zhengzhou 450001, Henan, China.
[3]Advanced Membranes and Porous Materials Center, Physical Sciences and Engineering Division, King Abdullah University of Science and Technology, Thuwal23955-6900, Saudi Arabia.
[4]Institut National de la Recherche Scientifique (INRS)-Energie Mat eriaux et Telecommunications, Varennes, QC J3X 1S2, Canada.
[5]Department of Physics, City University of Hong Kong, Hong Kong 999077, China.
[6]College of Chemistry and Molecular Sciences, Hubei Key Laboratory of Electrochemical Power Sources, Wuhan University, Wuhan 430072, Hubei, China.
[7]Yaoshan Laboratory, Pingdingshan 467000, Henan, China.
[#]Authors contributed equally.

[*]**Correspondence to:** Prof. Weihua Chen, College of Chemistry, Zhengzhou University, 100 Science Avenue, High-tech Zone, Zhengzhou 450001, Henan, China. E-mail: chenweih@zzu.edu.cn

## Methods

### Computation method of solid surface free energy

Solid surface free energy is an important parameter to evaluate the stability of materials, and several methods are used to calculate it, including dissolving heat method, tension method, splitting force method, theoretical estimation method and contact angle method. Contact angle method is the most commonly used method of estimating solid surface energy at present, possessing the advantages of simple operation and wide application. In the past few decades, many analytical models have been developed to compute surface energy from contact angles such as Fowkes, Owens Wendt Rabel and Kaelbel (OWRK), Van Oss-Chaudhury Good/Lewis acid base theory, Zisman and Neumann. In our work, the OWRK method suitable for universal systems has been adopted. The contact angel of solid materials is measured by sellile drop method.

Wetting phenomena can be illustrated according Young`s equation:

$\gamma_{lv}cos\theta = \gamma_{sv} - \gamma_{sl}$

In OWRK method, they separate the interfacial tension of liquid and surface energy of solid with two molecules, including dispersive interactions ($\gamma_{lv}^{D}$ and $\gamma_{sv}^{D}$) and polar interactions ($\gamma_{lv}^{P}$ and $\gamma_{sv}^{P}$). The combining rule provided by OWRK model is indicated below.

$\gamma_{sl} = \gamma_{sv} + \gamma_{lv} - 2(\sqrt{\gamma_{sv}^{D}\gamma_{lv}^{D}} + \sqrt{\gamma_{sv}^{P}\gamma_{lv}^{P}})$

We can get:

$\gamma_{lv}(1 + cos\theta) = 2(\sqrt{\gamma_{sv}^{D}\gamma_{lv}^{D}} + \sqrt{\gamma_{sv}^{P}\gamma_{lv}^{P}})$

In this equation, $\gamma_{sv}^{D}$ and $\gamma_{sv}^{P}$ are unknown. Firstly, at least two liquids with known dispersive and polar parts of surface tensions are needed. Then, contact angels of two liquids on the solid surface are tested. The value of $\gamma_{sv}^{D}$ and $\gamma_{sv}^{P}$ can be calculated.

$\gamma_{sv} = \gamma_{sv}^{D} + \gamma_{sv}^{P}$

So, the solid surface free energy ($\gamma_{sv}$) can be determined.

More detailed information of computation method of solid surface free energy is referred to literature.

### DFT computation Methods

All spin-polarized DFT calculations were performed under the general gradient approximation using the Perdew–Burke–Ernzerhof functionals as implemented in the

Vienna ab initio simulation package (VASP).[2, 3] The core-electrons were treated with the projector augmented wave method. The kinetic cutoff for plane-waves was set as 500 eV. For bulk calculations, a 2 × 2 × 3 supercell was used. DFT-D2 correction was added to describe the van der Waals interactions. The reciprocal space was sampled on a Monkhorst-Pack 10 × 10 ×10 meshes. The electron self-consistent calculations were converged to $10^{-4}$ eV. For structural relaxation, both the ion positions and the lattice parameters were allowed to change until the Hellman–Feynman forces on each ion went below $10^{-2}$ eV $Å^{-1}$. For the surface calculations, a slab model was built constituting three $SnS_2$ layers with a 2 × 2 periodic surface unit and the single graphene layer with a 3×3 supercell. To avoid self-interaction of the slab, a vacuum of 15 Å was used. The reciprocal space was sampled on a Monkhorst-Pack 7 × 7 × 1 meshes. The structural relaxation was performed in the same way as the bulk calculation, except the in-plane lattice parameters which were fixed at a serial of values around the bulk value of $SnS_2$ and the lowest-lying one in energy was selected. The diffusion barriers of $Na^+$ ions were calculated using the climb-image nudged elastic band theory. The initial band was constructed by linear interpolation of seven images. For the convergence of the elastic band, a force convergence of $10^{-2}$ eV $Å^{-1}$ was used.

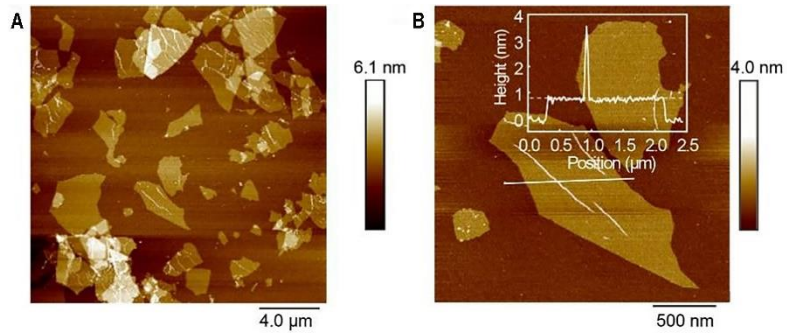


**Supplementary Figure 1.** Structural characterization of GO. (A) AFM image and (B) height profiles (inset image) of obtained GO raw materials[1]. The white lines represent the existence of folds due to GO sheets are hard to completely spread on the substrate.

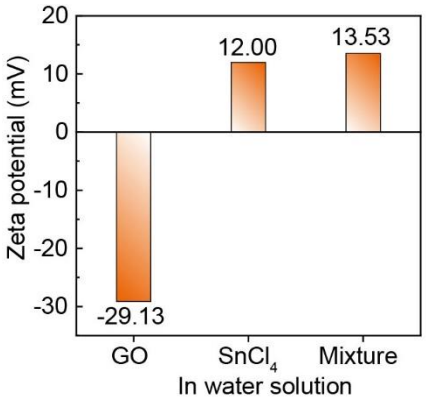


**Supplementary Figure 2.** Zeta potential of GO, $SnCl_4$ and their mixture in water.

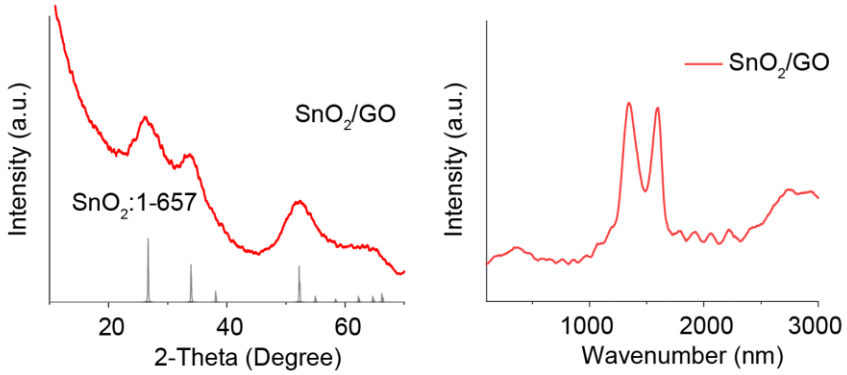


**Supplementary Figure 3.** XRD and Raman spectra of $SnO_2$/GO.

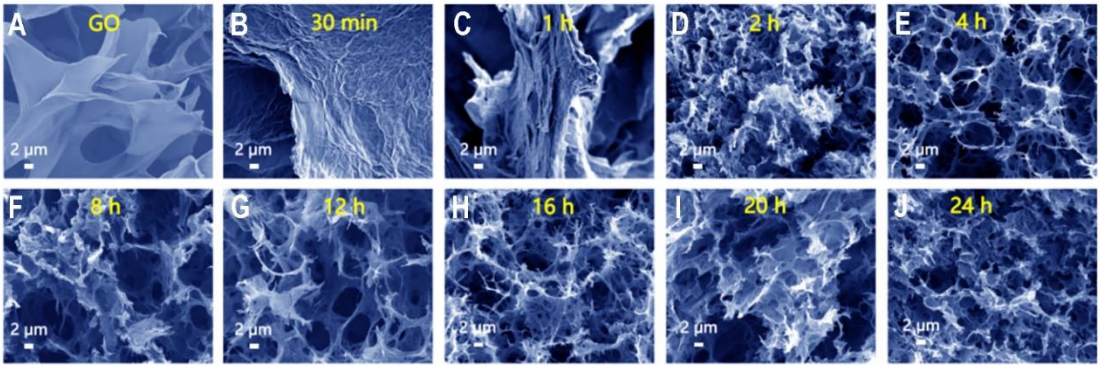


**Supplementary Figure 4.** (A-J) SEM images of GO at 0 min, 30 min, 1 h, 2 h, 4 h, 8 h, 12 h, 16 h, 20 h, 24 h.

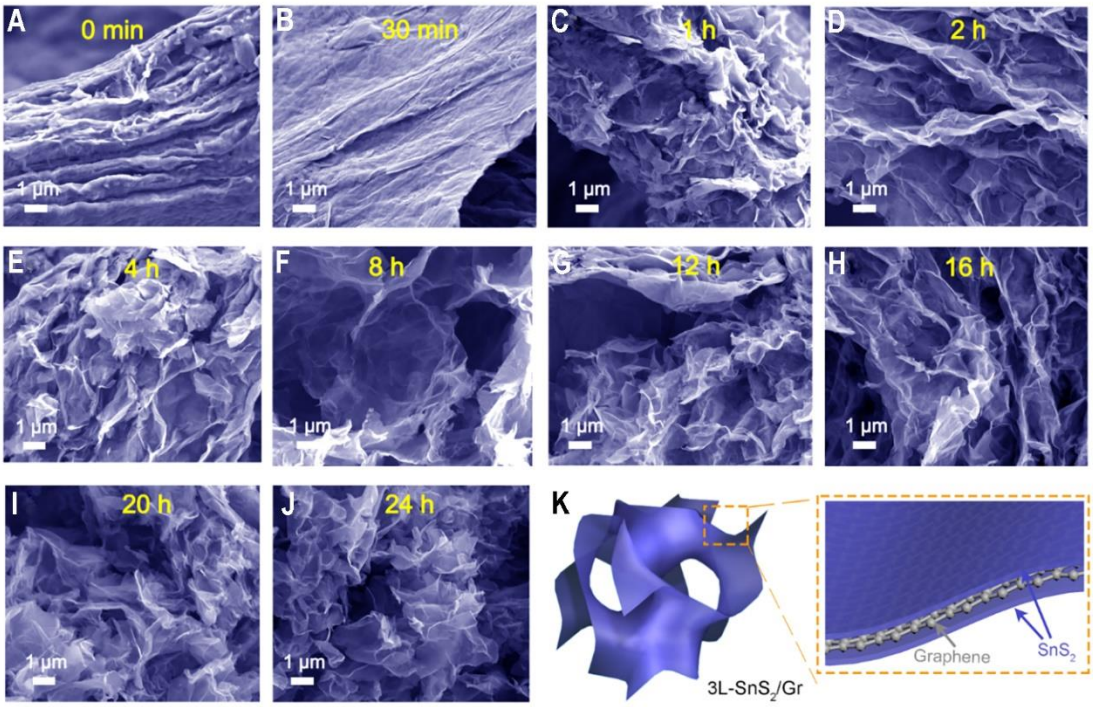


**Supplementary Figure 5.** (A-J) SEM images of 3L-$SnS_2$/Gr at 0 min, 30 min, 1 h, 2 h, 4 h, 8 h, 12 h, 16 h, 20 h, 24 h; (K) schematic illustration of 3L-$SnS_2$/Gr.

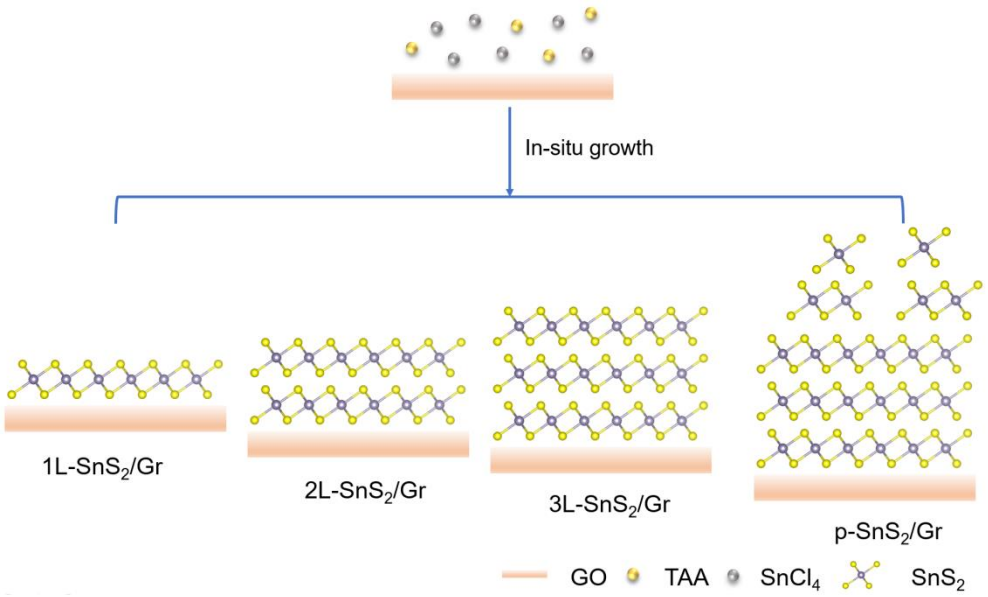


**Supplementary Figure 6.** Synthetic process of 1L-$SnS_2$/Gr, 2L-$SnS_2$/Gr, 3L-$SnS_2$/Gr and p-$SnS_2$/Gr.

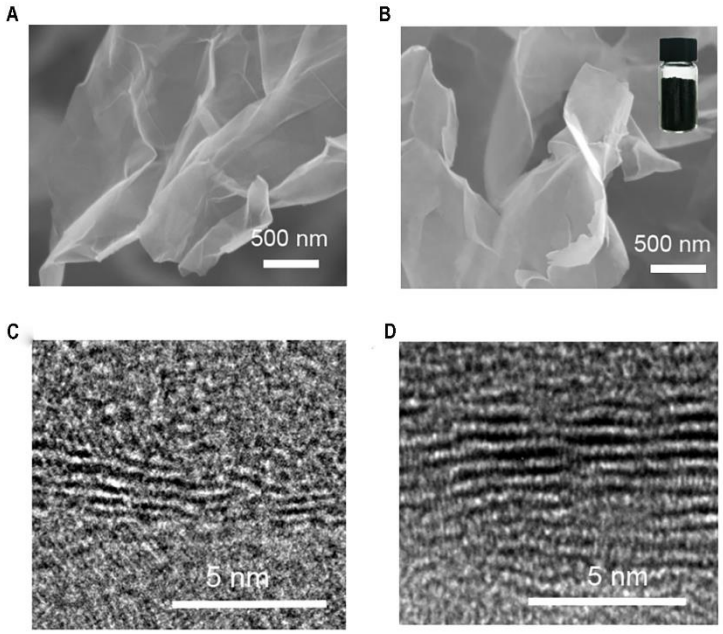


**Supplementary Figure 7.** (A and B) SEM images of 2L-$SnS_2$/Gr and 3L-$SnS_2$/Gr, inset of b the photograph of 3L-$SnS_2$/Gr; (C and D) TEM images of 2L-$SnS_2$/Gr and 3L-$SnS_2$/Gr.

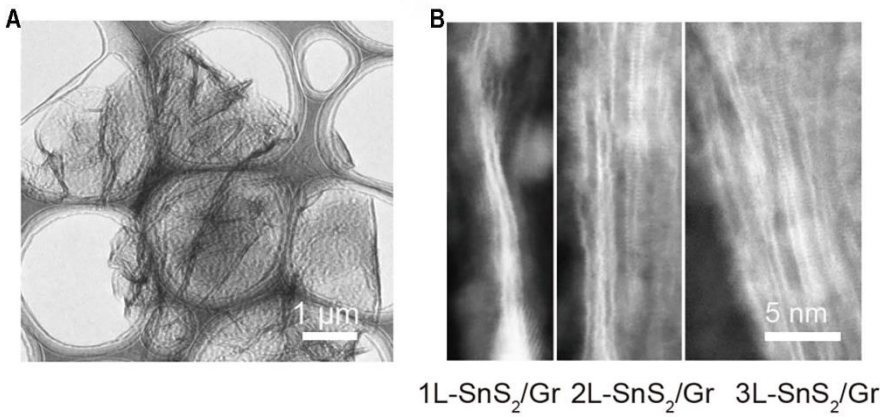


**Supplementary Figure 8.** (A) TEM image of 1L-$SnS_2$/Gr; (B) HAADF-STEM images of 1L-$SnS_2$/Gr, 2L-$SnS_2$/Gr and 3L-$SnS_2$/Gr.

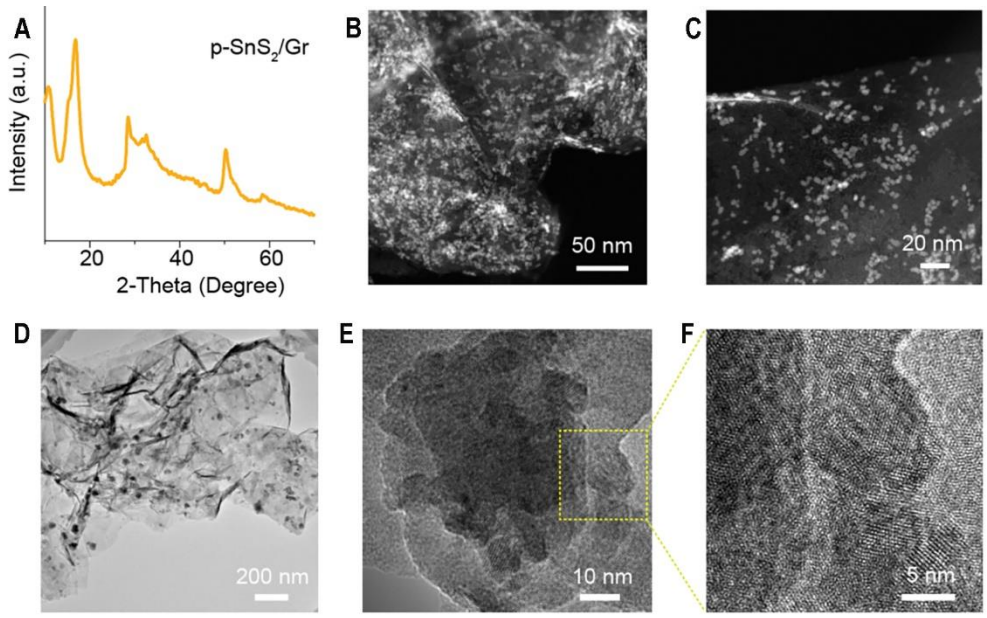


**Supplementary Figure 9.** Structural characterization of p-$SnS_2$/Gr. (A) XRD pattern; (B and C) HAADF-STEM images; (D) TEM image; (E and F) HRTEM images.

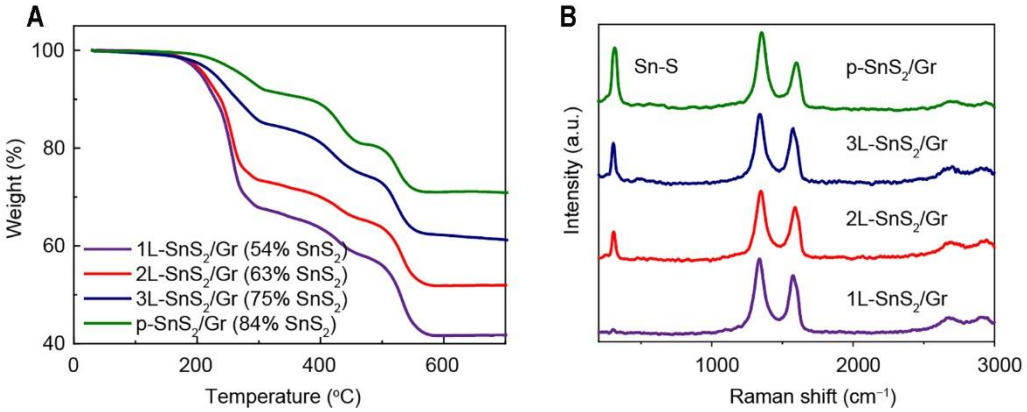


**Supplementary Figure 10.** (A) TGA curves and (B) Raman spectra of 1L-$SnS_2$/Gr, 2L-$SnS_2$/Gr, 3L-$SnS_2$/Gr and p-$SnS_2$/Gr.

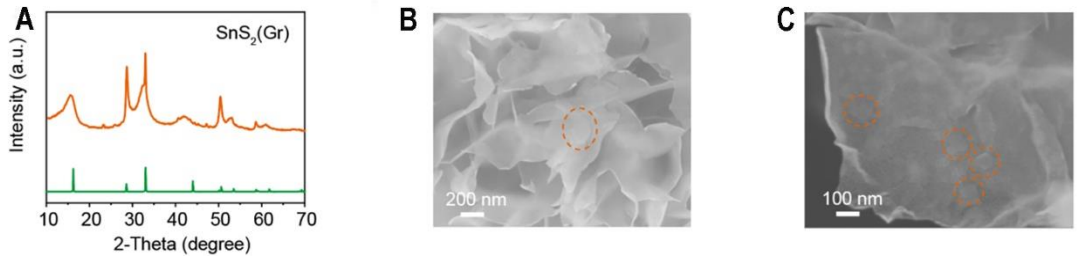


**Supplementary Figure 11.** (A) XRD of $SnS_2$(Gr); (B and C) SEM images of $SnS_2$(Gr).

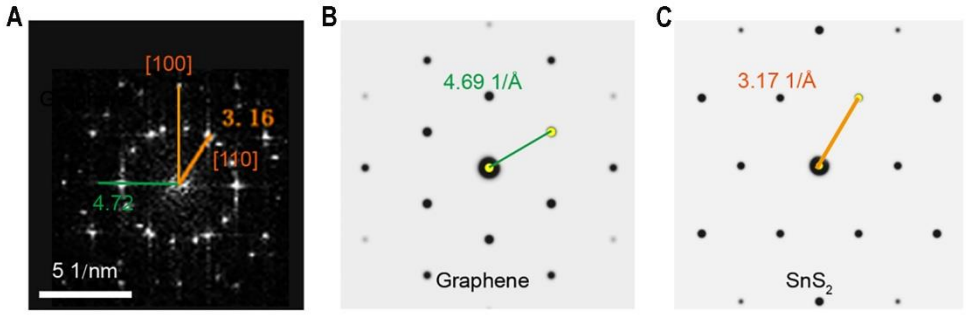


**Supplementary Figure 12.** (A) FFT image of 3L-$SnS_2$/Gr; (C and D) Calculated SAED images of graphene and $SnS_2$.

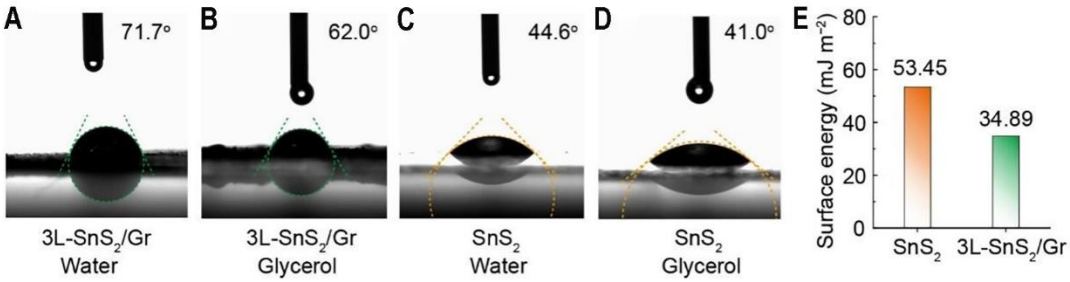


**Supplementary Figure 13.** Surface energy calculation of pure $SnS_2$ and as-obtained 3L-$SnS_2$/Gr. (A and B) Contact angles of as-obtained 3L-$SnS_2$/Gr in the water and glycerol; (C and D) Contact angles of pure $SnS_2$ in the water and glycerol; (E) Surface energy of pure $SnS_2$ and 3L-$SnS_2$/Gr.

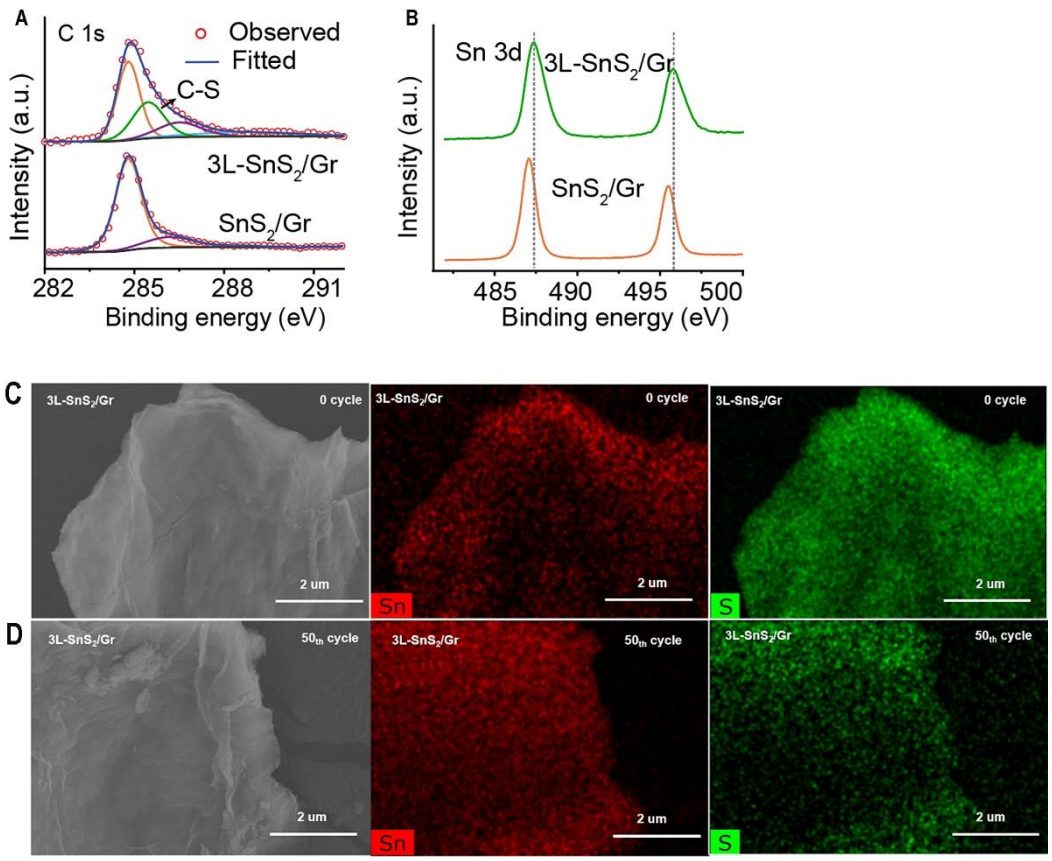


**Supplementary Figure 14.** (A and B) High resolution C 1s and Sn 3d spectra of 3L-$SnS_2$/Gr and $SnS_2$/Gr; (C and D) The SEM and EDS images of 3L-$SnS_2$/Gr at 0 cycle and 50 cycle comparison.

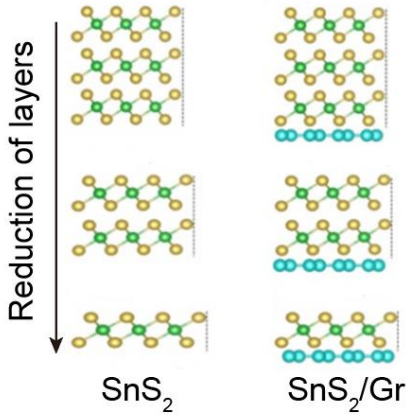


**Supplementary Figure 15.** (A) Schematic illustration of $SnS_2$ and $SnS_2$/Gr with reduction of layers.

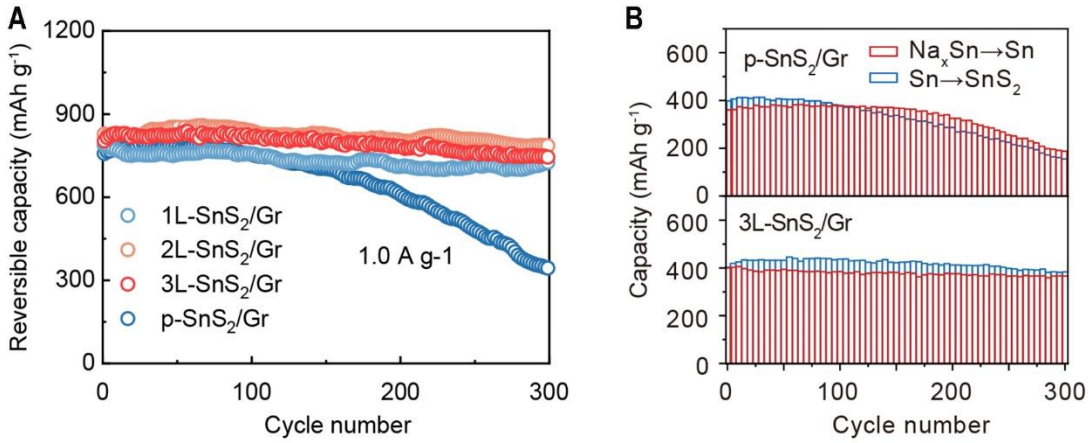


**Supplementary Figure 16.** (A) Cycling stability of 1L-$SnS_2$/Gr, 2L-$SnS_2$/Gr and 3L-$SnS_2$/Gr; (B) Capacity analysis of conversion and alloy reaction for 3L-$SnS_2$/Gr and p-$SnS_2$/Gr.

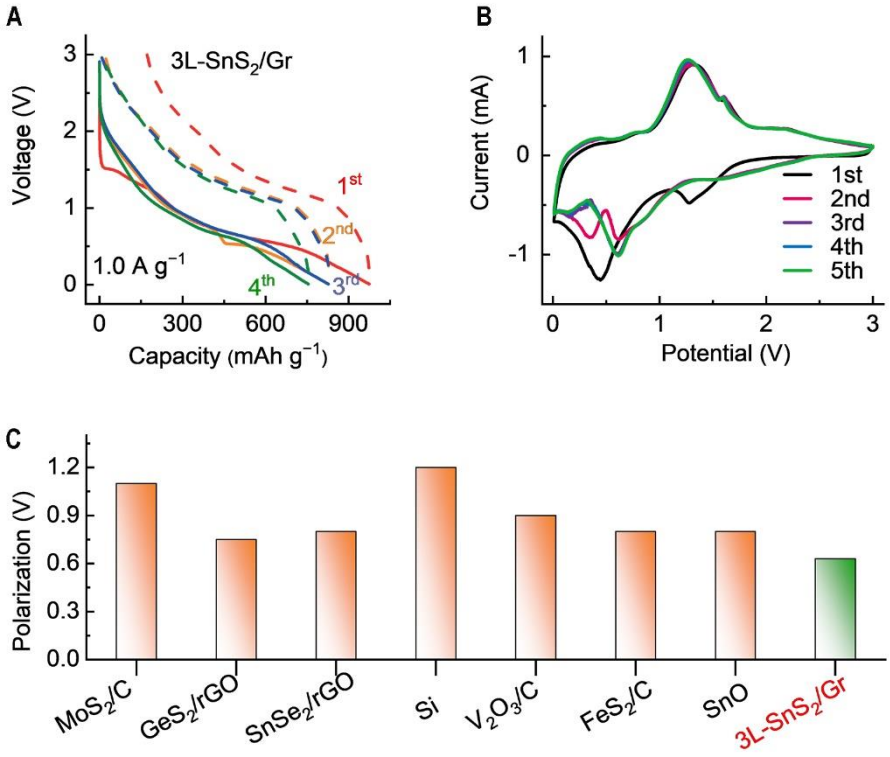


**Supplementary Figure 17.** Discharge/charge curve and midpoint voltage difference. (A) discharge/charge curve of 3L-$SnS_2$/Gr at 1.0 A $g^{-1}$; (B) CV of 3L-$SnS_2$/Gr at 1-5 cycles; (C) Potential voltage difference of various anode material[2, 3, 4, 5, 6, 7, 8] in SIBs.

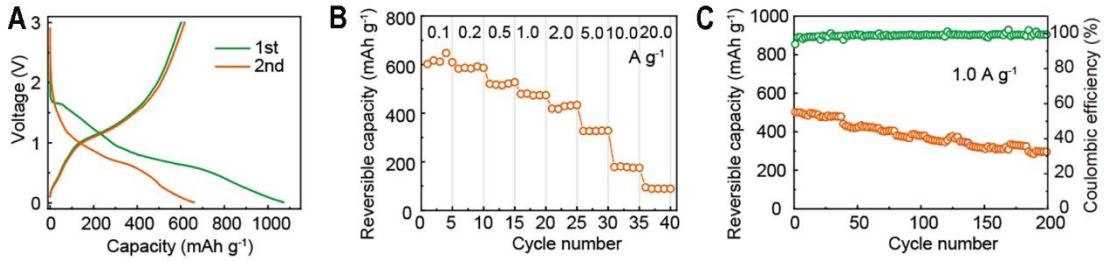


**Supplementary Figure 18.** (A) Charge/discharge curves; (B) rate performance; (C) cycling stability of $SnS_2$/Gr.

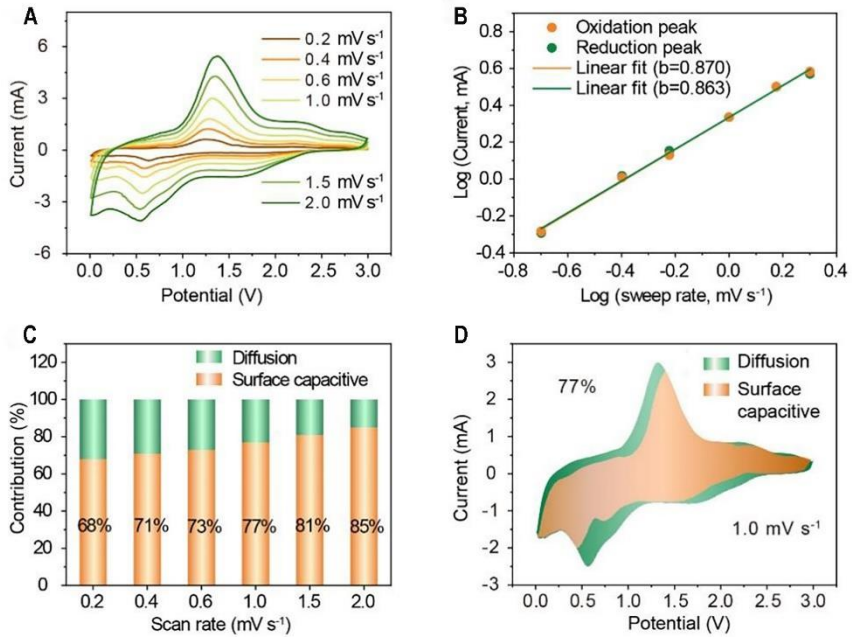


**Supplementary Figure 19.** Electrochemical reaction kinetics analysis of as-obtained 3L-$SnS_2$/Gr electrode. (A) CV curves of 3L-$SnS_2$/Gr at various scan rates for 0.2−2.0 mV $s^{-1}$; (B) Determination of the b-value using the relationship between anodic/cathodic peak current and scan rate; (C) surface capacitive contribution in 3L-$SnS_2$/Gr at various scan rates; (D) Separation of the capacitive and diffusion currents in 3L-$SnS_2$/Gr at a scan rate of 1.0 mV $s^{-1}$, respectively.

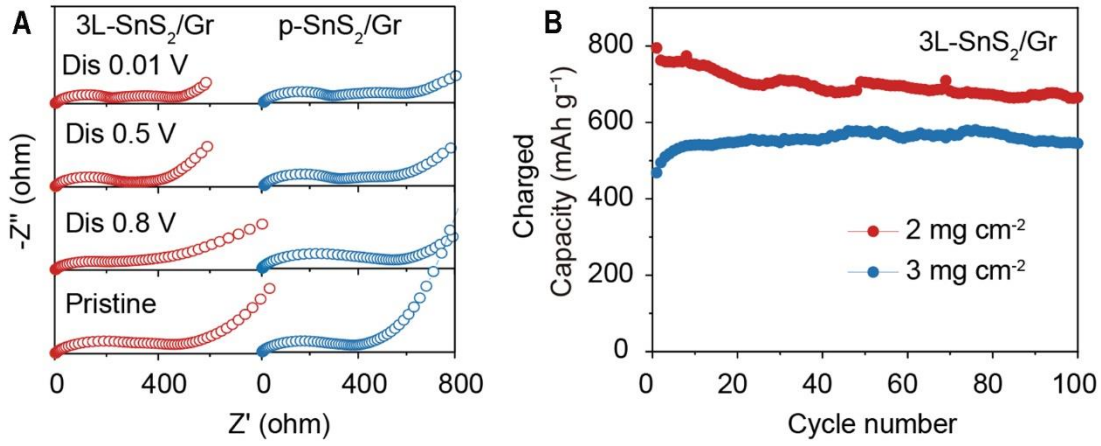


**Supplementary Figure 20.** (A) EIS spectra for 3L-$SnS_2$/Gr and p-$SnS_2$/Gr at pristine state, discharging to 0.8 V, 0.5 V, and 0.01 V; (B) Cycling stability of 3L-$SnS_2$/Gr at different loading content.

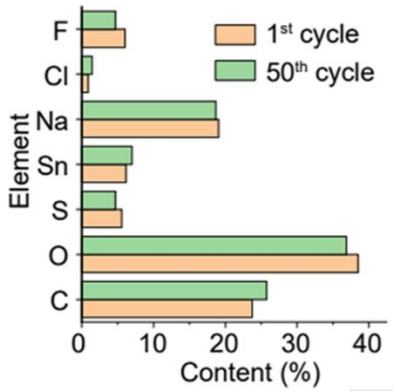


**Supplementary Figure 21.** The elements content comparation of SEI on the 3L-$SnS_2$/Gr after 1 cycle and 50 cycles.

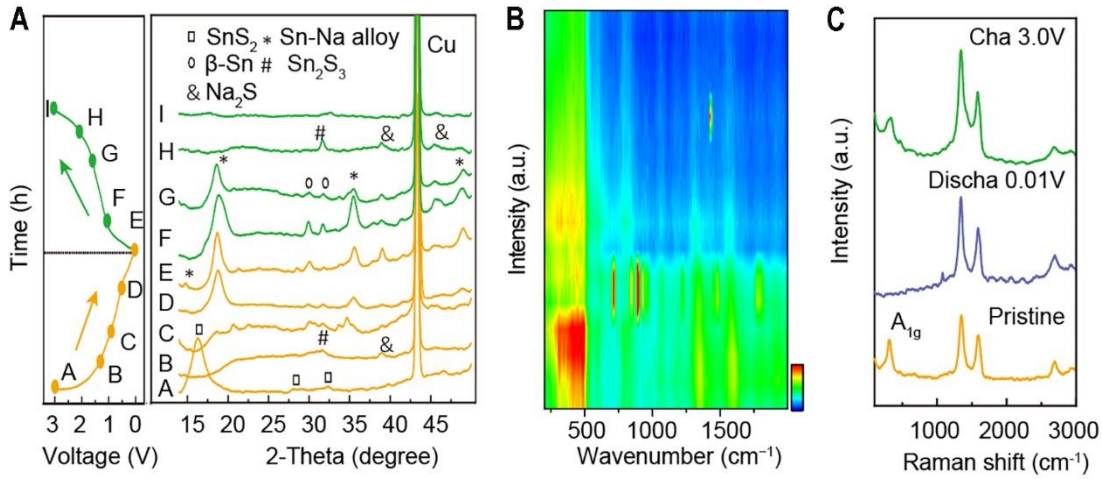


**Supplementary Figure 22.** (A) *Ex-situ* XRD patterns collected at various voltage; (B) *In-situ* Raman spectra during discharging process; (C) *Ex-situ* Raman spectrum of

the electrode before cycling, after first discharge to 0.01 V and after first charge to 3.0 V.

**Supplementary Table 1. Comparison of electrochemical performance of different anode materials in sodium-ion batteries**

| **Materials** | **Reversible capacity (mAh $g^{-1}$) at low current densities** | **High rate capacity (mAh $g^{-1}$)** | **Reversible capacity after long cycle (mAh $g^{-1}$)** | **Decay per cycle** |
|---|---|---|---|---|
| 3L-$SnS_2$/Gr | 953 (0.1 A $g^{-1}$) | 686 (5 A $g^{-1}$)<br>569 (10 A $g^{-1}$)<br>264 (30 A $g^{-1}$) | 549 (10 A $g^{-1}$, 600 cycles) | 0.005% |
| $SnS_2$@CNT[9] | 523 (0.1 A $g^{-1}$) | 441 (5 A $g^{-1}$) | 525 (0.2 A $g^{-1}$, 100 cycles) | 0.25% |
| CoSe–rGO[10] | 491 (0.1 A $g^{-1}$) | 267 (20 A $g^{-1}$) | 401 (1 A $g^{-1}$, 100 cycles) | 0.118% |
| $GeS_2$/rGO[11] | 783 mAh $g^{-1}$ (0.1 A $g^{-1}$) | 616 (5 A $g^{-1}$) | 720 (0.1 A $g^{-1}$, 100 cycles) | 0.106% |
| $MoS_2$-rGO/HCS[3] | 646 (0.1 A $g^{-1}$) | 364 (5 A $g^{-1}$) | 443 (1.0 A $g^{-1}$, 500 cycles) | 0.015% |
| $VS_4$[12] | 580 (0.1 A $g^{-1}$) | 173 (10 A $g^{-1}$) | 402 (0.5 A $g^{-1}$, 300 cycles) | 0.007% |
| $Fe_3N$@C[13] | 356 (0.1 A $g^{-1}$) | 248 (2.0 A $g^{-1}$) | 280 (0.4 A $g^{-1}$, 300 cycles) | 0.04% |
| SnS@C nanotubes[14] | 450 (0.1 A $g^{-1}$) | 290 (5 A $g^{-1}$) | 469 (0.2 A $g^{-1}$, 100 | 0.09% |

| | | | | |
|---|---|---|---|---|
| | | | cycles) | |
| $SnS_2$/GCA[15] | 630 (0.2 A $g^{-1}$) | 301 (10 A $g^{-1}$) | 260 (3 A $g^{-1}$, 1000 cycles) | 0.03% |
| FeS@$Fe_3C$@ Graphitic[16] | 750 (0.1 A $g^{-1}$) | 292 (5 A $g^{-1}$) | 575.7 (0.1 A $g^{-1}$, 200 cycles) | 0.28% |
| $Sb_2S_5$-GF[7] | 843 (0.1 A $g^{-1}$) | 525 (10.0 A $g^{-1}$) | 748 (0.2 A $g^{-1}$, 300 cycles) | 0.028% |
| SnSe NS[17] | 400 (0.1 A $g^{-1}$) | 106 (20.0 A $g^{-1}$) | 183 (2 A $g^{-1}$, 100 cycles) | 0.37% |
| $CoS_x$[18] | 800 (0.1 A $g^{-1}$) | 479 (2.0 A $g^{-1}$) | 572 (0.5 A $g^{-1}$, 100 cycles) | 0.17% |
| $FeS_2$@C[6] | 560 (0.1 A $g^{-1}$) | 403 (5 A $g^{-1}$) | 330 (2 A $g^{-1}$, 800 cycles) | 0.0425% |

**References:**


1. Jr. Hummers, W. S. & Offeman, R. E. Preparation of Graphitic Oxide. *J. Am. Chem. Soc.* 80, 1339 (1958). https://doi.org/10.1021/ja01539a017.

2. Harikesh, P. C. et al. Doping and Switchable Photovoltaic Effect in Lead-Free Perovskites Enabled by Metal Cation Transmutation. *Adv. Mater.* 30, 1802080 (2018). DOI: 10.1002/adma.201802080.

3. Hu, X. et al. Three-Dimensional Network Architecture with Hybrid Nanocarbon Composites Supporting Few-Layer MoS2 for Lithium and Sodium Storage. *ACS Nano* 12, 1592-1602 (2018). DOI: 10.1021/acsnano.7b08161.

4. Li, Y., Hu, Y., Titirici, M., Chen, L. & Huang, X. Hard Carbon Microtubes Made from Renewable Cotton as High-Performance Anode Material for Sodium-Ion Batteries. *Adv. Energy Mater.* 6, 1600659 (2016). DOI: 10.1002/aenm.201600659.

5. Zheng, Y. et al. Boosted Charge Transfer in SnS/$SnO_2$ Heterostructures: Toward

High Rate Capability for Sodium-Ion Batteries. *Angew. Chem. Int. Ed.* 55, 3408-3413 (2016). DOI: 10.1002/ange.201510978.
6. Liu, Z. et al. Structure-designed synthesis of $FeS_2$@C yolk–shell nanoboxes as a high-performance anode for sodium-ion batteries. *Energy Environ. Sci.* 10, 1576-1580 (2017). DOI: 10.1039/c7ee01100h.
7. Lu, Y. et al. High-Capacity and Ultrafast Na-Ion Storage of a Self-Supported 3D Porous Antimony Persulfide–Graphene Foam Architecture. *Nano Lett.* 17, 3668-3674 (2017). DOI: 10.1021/acs.nanolett.7b00889.
8. Ren, W., Zhang, H., Guan, C. & Cheng, C. Ultrathin MoS2 Nanosheets@Metal Organic Framework-Derived N-Doped Carbon Nanowall Arrays as Sodium Ion Battery Anode with Superior Cycling Life and Rate Capability. *Adv. Funct. Mater.* 27, 1702116 (2017). DOI: 10.1002/adfm.201702116.
9. Liu, Y. et al. Confining $SnS_2$ Ultrathin Nanosheets in Hollow Carbon Nanostructures for Efficient Capacitive Sodium Storage. *Joule* 2, 725-735 (2018). DOI: 10.1016/j.joule.2018.01.004.
10. Li, Y. et al. Stable Carbon–Selenium Bonds for Enhanced Performance in Tremella-Like 2D Chalcogenide Battery Anode. *Adv. Energy Mater.* 8, 1800927 (2018). DOI: 10.1002/aenm.201800927.
11. Kim, J., Yun, J. H. & Kim, D. K. A Robust Approach for Efficient Sodium Storage of $GeS_2$ Hybrid Anode by Electrochemically Driven Amorphization. *Adv. Energy Mater.* 8, 1703499 (2018). DOI: 10.1002/aenm.201703499.
12. Wang, S. et al. Graphene Oxide-Template Controlled Cuboid-Shaped High-Capacity VS4 Nanoparticles as Anode for Sodium-Ion Batteries. *Adv. Funct. Mater.* 28, 1801806 (2018). DOI: 10.1002/adfm.201801806.
13. Li, Z., Fang, Y., Zhang, J. & Lou, X. W. D. Necklace-Like Structures Composed of $Fe_3N$@C Yolk–Shell Particles as an Advanced Anode for Sodium-Ion Batteries. *Adv. Mater.* 30, 1800525 (2018). DOI: 10.1002/adma.201800525.
14. He, P., Fang, Y., Yu, X. & Lou, X. W. D. Hierarchical Nanotubes Constructed by Carbon-Coated Ultrathin SnS Nanosheets for Fast Capacitive Sodium Storage. *Angew. Chem. Int. Ed.* 56, 12202-12205 (2017). DOI: 10.1002/anie.201706652.
15. Cui, J. et al. Revealing Pseudocapacitive Mechanisms of Metal Dichalcogenide $SnS_2$/Graphene-CNT Aerogels for High-Energy Na Hybrid Capacitors. *Adv. Energy Mater.* 8, 1702488 (2018). DOI: 10.1002/aenm.201702488.
16. Wang, Q. et al. In Situ Construction of 3D Interconnected FeS@$Fe_3C$@Graphitic

Carbon Networks for High-Performance Sodium-Ion Batteries. *Adv. Funct. Mater.* 27, 1703390 (2017). DOI: 10.1002/adfm.201703390.
17. Yuan, S. et al. Surfactant-Free Aqueous Synthesis of Pure Single-Crystalline SnSe Nanosheet Clusters as Anode for High Energy- and Power-Density Sodium-Ion Batteries. *Adv. Mater.* 29, 1602469 (2017). DOI: 10.1002/adma.201602469.
18. Xiao, Y., Hwang, J., Belharouak, I. & Sun, Y. Superior Li/Na-storage capability of a carbon-free hierarchical $CoS_x$ hollow nanostructure. *Nano Energy* 32, 320-328 (2017). DOI: 10.1016/j.nanoen.2016.12.053.